Analysis of Electroosmotically Driven Micro-Channel Flows

By PRASHANTA DUTTA[1], TIMOTHY C. WARBURTON[2] AND ALI BESKOK[1]†

[1]Mechanical Engineering Department, Texas A&M University, College Station, TX 77843, USA

[2]Division of Applied Mathematics, Brown University, Providence, RI 02912, USA

(Received Draft)

Mixed electroosmotic/pressure driven flows are analyzed both numerically and analytically for two-dimensional micro-channels. The numerical approach is based on the spectral element methodology, which resolves the velocity distribution within the electric double layer with exponential (spectral) accuracy. Analytical relations for the wall shear stress, velocity and pressure distributions in the mixed electroosmotic/pressure driven channels are obtained. The electrokinetic pumping and the mechanism for creating large pressure gradients with zero mass flowrate are demonstrated. These two effects can be utilized in designing various micro-fluidic systems with no moving components. Finally, a "slip boundary condition" which incorporates effects of the electric double layer on the velocity distribution is introduced. The advantages and disadvantages of utilizing such a slip condition are discussed.

1. Introduction

Recent developments in micro-fabrication technologies enabled a variety of miniaturized fluidic systems consisting of micro-ducts, valves, pumps and various other injection systems. These micro-fluidic devices can be utilized in medical, pharmaceutical and defense applications, for example in drug delivery, DNA analysis and sequencing and biological/chemical agent detection sensors on micro-chips. The main advantages of these emerging micro-fluidic technologies are their low-cost, light-weight and small-size.

The technological demands on micro-fluidic systems require a better understanding of the micro-scale thermal/fluidic transport phenomena, which differ from their larger-scale counterparts mainly due to the size and the surface force effects (Ho & Tai, 1998; Gad-el-Hak, 1999). For devices smaller than one millimeter in length, the surface forces are more dominant than the body forces. Considering that all of the micro-scale systems work in gas or liquid environments, the fluid forces on these systems rank the second after the surface to surface contact forces (Gabriel, Jarvis & Trimmer, 1998). The origin of the fluid forces on surfaces is the interactions between the liquid or gas molecules with the surface atoms. This interaction is based on the short-ranged van der Waals forces and longer ranged electrostatic or Coulombic forces (Ho & Tai, 1998; Gad-el-Hak, 1999). Gas flows in micro-scales also exhibit rarefaction effects due to the gas mean free path being comparable with the characteristic flow length scales (for details about the rarefaction effects on gas micro-flows see Beskok & Karniadakis, 1999; Beskok, Trimmer & Karniadakis, 1996).

† Author to whom correspondence should be addressed

In this paper we examine the electrokinetic effects; mainly the behavior of an ionized fluid near a charged surface. According to Probstein (1994), the electrokinetic effects have been first described by F.F. Reuss in 1809. This was followed later by the seminal work of Helmholtz (1879) on the electric double layer theory, which related the electrical and flow parameters for electrokinetic transport. The electrokinetic phenomenon can be divided into four parts (Probstein, 1994):

- Electroosmosis: Motion of ionized liquid relative to the stationary charged surface by an applied electric field. This part is the main emphasis of the current paper.
- Electrophoresis: Motion of the charged surface relative to the stationary liquid by an applied electric field.
- Streaming Potential: Electric field created by the motion of ionized fluid along stationary charged surfaces (opposite of electroosmosis).
- Sedimentation Potential: Electric field created by the motion of charged particles relative to a stationary liquid (opposite of electrophoresis).

Here in this paper, we demonstrate utilization of electrokinetic forces for pumping liquids. This leads to the concept of building micro-pumps with non-moving components. Such pumps will not be prone to mechanical failure due to fatigue. Moreover, they will be more advantageous for biomedical applications, since cell damage due to pumping will be minimized, compared to the micro-pumps with moving valves, blades and pistons.

Since the discovery of the electrokinetic phenomenon there has been numerous analytical, experimental, and numerical studies of this phenomenon. In early 1900's von Smoluchowski made seminal contributions to our understanding of electrokinetically driven flows, especially for conditions where the electric double layer thickness is much smaller than the channel height. In the later part of the 20^{th} Century, Burgreen & Nakache (1964) presented a seminal analysis of mixed electroosmotic/pressure driven channel flow for very thin two-dimensional channels. In their analysis the channel height was comparable to the electric double layer thickness. This work was followed by a theoretical analysis of electrokinetic flows in thin cylindrical capillaries by Rice & Whitehead (1965), and later by Keh and Liu (1995).

In a recent experimental and numerical simulation work, Molho *et al.*(1998) presented results for electrokinetically driven flows in micro-capillaries, with emphasis on microfluidic applications. In their study, the effects of Joule heating and the corresponding changes in the fluid viscosity are shown to be secondary effects, compared to the streamwise pressure gradients. The same year Paul, Garguilo & Rakestraw (1998) have used ultraviolet laser pulses to capture the flow patterns in mixed electrokinetic/pressure driven micro-channel flows using a caged dye fluorescence technique. Very high resolution images of the flow field were obtained. Later, a combined experimental and theoretical analysis of electroosmotic flows is presented by Cummings, Griffiths & Nilson (1999). They used micro particle image velocimetry (μPIV) technique to obtain the velocity distribution for straight channels and for crossing of two micro-channels. Cummings *et al.*(1999) have also introduced the "ideal electroosmosis" concept, which reduces the flow field outside the electric double layer to a potential flow. However, this condition is valid under some *specific* outer field boundary conditions, which does not necessarily apply to our analysis in the following sections. Most recently, Herr *et al.*(2000) performed velocity and dispersion rate measurements on electroosmotic flows through cylindrical capillaries with nonuniform surface charge distribution. The experimental results, performed by caged-dye fluorescense technique indicated strong dependence of fluid velocity and dispersion rate on the surface charge.

The past decade has witnessed various numerical modeling and simulation efforts. For example, Yang and Li (1998) have used the Debye-Hückel approximation to develop a nu-

merical algorithm for elecrokinetically driven liquid flows. This is followed by forced convection heat transfer study in micro-channels, including the electrokinetic effects (Yang, Li & Masliyah, 1998), where the authors have rigorously identified the streaming potential effects and offered an explanation for deviations from the Poiseulle flow results for micro-scale liquid flows, first reported by Pfahler *et al.*(1991); (also see Wilding *et al.*, 1994).

Numerical simulations of micro-fluidic injection using electroosmotic forces through intersection of two channels is presented by Patankar & Hu (1998) by using the Debye-Hückel linearization. A numerical algorithm for electroosmotic and electrophoretic transport and species diffusion has also been developed by Ermakov, Jacobson & Ramsey (1998) for two-dimensional complex geometry flow conduits. In the meantime, Lyklema, Rovillard & DeConnick (1998) have used molecular dynamics method to simulate the ion distribution very near the charged surfaces. The molecular interactions were modeled by the Lennard-Jones potential. Interactions of the wall, solvent and solute molecules in six different combinations were modeled with different Lennard-Jones coefficients. The results of Lyklema *et al.*(1998) confirm the presence of a stagnant layer of fluid very near the surfaces. This is primarily due to the interaction of fluid ions with the oppositely charged surface. This layer is also known as the "stern layer", and it is typically about a few ion-diameter thick (Probstein, 1994).

In regards to the recent applications of the electroosmotic phenomenon, Jacobson, Ermakov & Ramsey (1999) have obtained parallel and serial mixing mechanisms in micro-capillary networks, and have shown that parallel mixing devices increase the reliability of micro-fluidic systems. In a set of experiments, Polson & Hayes (2000) have demonstrated flow control by using the electroosmotic forces. Meanwhile, Dahm, Diez-Garias & Paul (2000) used the electrokinetic pumping technology to design micro-actuator arrays for turbulent boundary layer control via micro-nozzle jets .

Considering the difficulties associated with performing experiments in micro-scales, it is desirable to develop reliable numerical models, which accurately describe the electrokinetically driven flows in complex micro-geometries. These numerical models can provide a further understanding of *coupled effects of the pressure, surface, inertial and electrokinetic forces* on fluid motion, and hence can be utilized for an optimized micro-fluidic system design prior to the hardware fabrication and experimental verification.

This paper is organized as follows: In section 2, the electric double layer concept is introduced. Starting from the ion transport equation, the governing equations for the electric charge distribution is derived. In section 3, the governing equations for the electroosmotically driven flows are presented with details about the underlying assumptions and approximations. The numerical algorithm used in the analysis of the problem, grid resolution and numerical accuracy issues are also addressed. In section 4, the mixed electroosmotic/pressure driven channel flow problem is studied analytically. In section 5, numerical simulation results are presented and compared with the analytical formulas. Also, a velocity slip condition, which incorporates effects of the electric double layer on the velocity distribution is introduced. The advantages and disadvantages of utilizing such a slip condition are discussed. In section 6, streaming potential effects on the net streamwise electric field is derived. Hence, the analytical relations and the experimental data can be correlated. Finally in section 7, a summary of our findings and the directions of our future work are presented.

2. Electric Double Layer

A dilute solution in contact to a surface with trapped surface charge experiences redistribution of its ions, resulting in formation of the electric double layer (EDL); (see Probstein, 1994). The governing equations for the ion density distribution within the EDL can be derived starting from the species conservation equation written for the j^{th}-type ions in the following form:

$$\frac{\partial n_j}{\partial t} + \nabla.(\vec{V}_j n_j) = \nabla.(D_j \nabla n_j) + R_j, \tag{2.1}$$

where n_j, D_j and R_j are the ion-density (ion-concentration), diffusion coefficient, and the source terms, respectively. The subscript j indicates the ion type. This equation is known as the Nerst-Plank equation and includes convection and diffusion of the species. In this paper we will analyze steady Nerst-Plank equation in the absence of source terms. The term $\nabla.(\vec{V}_j n_j)$ in equation (2.1) shows convection of the j^{th}-type ions with total velocity $\vec{V}_j$, which can be decomposed into two parts

$$\vec{V}_j = \vec{V} + \vec{v}_j, \tag{2.2}$$

where $\vec{V}$ is the velocity field due to the hydrodynamic base-flow, and $\vec{v}_j$ is the velocity field due to the electrostatic force $\vec{F}_j$ acting on the ions in the presence of surface charges. The velocity $\vec{v}_j$ is proportional to the electrostatic force

$$\vec{F}_j = R_{hj}\vec{v}_j, \tag{2.3}$$

where R_{hj} is the hydrodynamic resistance coefficient for the j^{th} type ions. The above equation assumes *zero relaxation time* for the ion velocity $\vec{v}_j$. A valid approximation for steady or quasi steady electrostatic force field. The resistance coefficient R_{hj} is determined by the Stokes-Einstein equation

$$R_{hj} = k_b T/D_j, \tag{2.4}$$

where k_b is the Boltzmann constant, and T is the fluid temperature. The electrostatic force $\vec{F}_j$ can be represented as a function of an electrostatic field $\vec{E} = -\nabla\psi$ in the following form:

$$\vec{F}_j = ez_j\vec{E} = -ez_j\nabla\psi, \tag{2.5}$$

where e and z_j are the electron charge and valence for the j^{th} type ion, respectively.

Using equations (2.3-2.5) we can represent the velocity $\vec{v}_j$ in the following form:

$$\vec{v}_j = -\frac{ez_j D_j \nabla\psi}{k_b T} = -\alpha D_j \nabla(\psi/\psi_o), \tag{2.6}$$

where $\alpha = ez\psi_o/k_bT$ is the ionic energy parameter, and ψ_o is the *surface electric potential*. For simplicity we normalized the electric potential ψ with the surface electric potential, i.e. $\psi^* = \psi/\psi_o$. Using equation (2.6) and the divergence free hydrodynamic velocity (i.e. $\nabla \cdot \vec{V} = 0$), equation (2.1) can be simplified in the following form:

$$\nabla^2(D_j n_j) = \nabla.(-n_j \alpha D_j \nabla\psi^*) + \vec{V}.\nabla n_j. \tag{2.7}$$

Assuming a constant ion-diffusion coefficient D_j we obtain

$$D_j\nabla^2(n_j) + D_j\nabla.(n_j\alpha\nabla\psi^*) = \vec{V}.\nabla n_j. \tag{2.8}$$

The right-hand side of this equation shows convection of ions due to the hydrodynamic

flow field, and couples the ion distribution equation with the Navier-Stokes equations. For micro-channel flows the Reynolds number is small. Therefore, the developing flow region at the channel inlet can be neglected and the velocity field can be assumed fully developed in the entire channel. On the other hand, for complex geometry flows the ion-convection effects can be predicted by using the Peclet number based on the Schmidt number ($Pe = Re * Sc$, where Re and Sc are the Reynolds and Schmidt numbers, respectively). If the Peclet number is smaller than unity then the ion-convection can be neglected to some extend. Most of the micro-fluidic applications are in the Stokes flow regime where $Re \simeq 0.001$. For such cases $Sc \simeq 100$ will result in $Pe < 1$. Under these conditions the ion-convection effects will be relatively smaller than the ion diffusion effects, and their contribution to equation (2.8) can be neglected. Keeping this in mind, we drop the ion-convection terms in equation (2.8), and obtain

$$\nabla.(\nabla n_j) = \nabla.(-n_j \alpha \nabla \psi^*). \tag{2.9}$$

This simplification is crucial for effective analytical treatment of the electroosmotic flows.

For channel flows, the electrostatic potential is symmetric with respect to the channel center, and variations exist only in the cross-flow direction. Hence equation (2.9) can be integrated twice resulting in

$$n_j = n_{jo} exp(-\alpha \psi^*), \tag{2.10}$$

where n_{jo} is the concentration of the j^{th}-type ions sufficiently away from the electric double layer, for example at the channel center. The equation (2.10) shows a Boltzmann distribution for the ion density. This result is in agreement with the derivation based on statistical mechanical considerations (Feynman *et al.*, 1977). If we use simple electrolytes that dissociate into two equally charged ions of valence z and $-z$, the net charge density per unit volume of the fluid (ρ_e) is given as:

$$\rho_e = -2 n_o e z sinh(\alpha \psi^*), \tag{2.11}$$

where n_o is the ion concentration in the bulk solution for both positively and negatively charged ions. This charge density and the electric potential distribution ψ^* are related by the following Poisson-Boltzmann equation (Adamson, 1990; Probstein, 1994):

$$\nabla^2(\psi^*) = \frac{-4\pi h^2 \rho_e}{D \psi_o} = \beta sinh(\alpha \psi^*), \tag{2.12}$$

where the spatial gradients are non-dimensionalized with a characteristic length h and the parameter β relates the ionic energy parameter α and the characteristic length h to the Debye-Hückel parameter ω as shown below

$$\beta = \frac{(\omega h)^2}{\alpha},$$

$$\omega = \frac{1}{\lambda} = \sqrt{\frac{8\pi n_o e^2 z^2}{D k_b T}}. \tag{2.13}$$

The solution of equation (2.12) gives the electric potential distribution ψ^*, which decays exponentially fast within the electric double layer (EDL). The thickness of EDL is known as the Debye length $\lambda = 1/\omega$. Most of the electric charge is concentrated within the EDL. The Debye length is a function of the ion density n_o. For aqueous solutions at 25^oC , the ion densities of $1 mol/m^3$ and $100 mol/m^3$ correspond to the Debye lengths of $\lambda = 10nm$, and $\lambda = 1nm$, respectively.

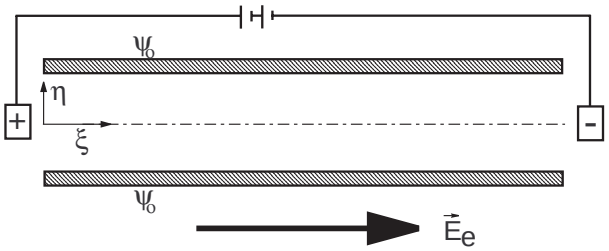

FIGURE 1. Schematic view of the elecroosmotic flow between two parallel plates. The electric charge potential on the wall is shown by ψ_o, and the external electric field is indicated by $\vec{E}_e$.

For our analysis we consider a two dimensional channel as shown in figure 1. We assume that the wall potential ψ_o is known, and it remains constant along the channel. Under these conditions we simplify equation (2.13) in the following form:

$$\frac{d^2\psi^*}{d\eta^2} = \beta sinh\left(\alpha\psi^*\right), \tag{2.14}$$

where $\eta = y/h$ and h is the half channel height. If we multiply both sides of this equation by $2\frac{d\psi^*}{d\eta}$, and integrate with respect to η we obtain the following relation:

$$\frac{d\psi^*(\eta)}{d\eta} = (\frac{\omega h}{\alpha})\left[2cosh(\alpha\psi^*) - 2cosh(\alpha\psi_c^*)\right]^{\frac{1}{2}}, \tag{2.15}$$

where both the electric potential and its spatial gradient at point η is represented as a function of the electric potential at the channel center (i.e., $\psi_c^* = \psi_{\eta=0}^*$).

An analytical solution of (2.14) was obtained by Burgreen and Nakache (1964) in terms of a first-kind elliptic integral. Their work presents the potential distribution as a function of the Debye length λ and the ionic energy parameter α. In figure 2, we present the numerical solution of the potential distribution as a function of various α and β. The top figure shows the potential distribution for $\alpha = 1$. For small values of β, the electric double layer is very thick and it covers the entire channel. As the value of β is increased the electric double layer is confined to the channel walls, resulting in sharp variations in the electric potential. For $\beta = 100$, the electric double layer covers about 20% of the channel. The electric potential distribution for $\alpha = 10$ is shown in the lower part of figure 2. For a fixed value of β, comparisons of $\alpha = 1$ in the top figure and $\alpha = 10$ in the bottom figure shows even faster decay of the electric potential for larger values of α.

For $\alpha \geqslant 1$ and $\beta \geqslant 100$ the electric potential at the middle of the channel is practically zero as seen in figure 2. When $\psi_c^* = 0$ the last term in equation (2.15) is simplified, and using the identity $\cosh(p) = 2\sinh^2(p/2) + 1$, equation (2.15) can be integrated once more. This results in the following form:

$$\psi^*(\eta) = \frac{4}{\alpha}\tanh^{-1}\left[\tanh\left(\frac{\alpha}{4}\right)\exp\left(-\sqrt{\alpha\beta}\ \ \eta^*\right)\right], \tag{2.16}$$

where, η^* is the distance from the wall (i.e, $\eta^* = 1 - |\eta|$). Here we must emphasize two important limitations. The first one is that equation (2.16) gives the potential decay from the wall, and assumes that the two walls do not interact. This condition is satisfied if $\psi_c^* = 0$. The second condition is for large value of α, such as $\alpha \geqslant 50$, where evalution of the potential on the wall ($\eta^* = 0$) can become problematic, since $\tanh^{-1}(1) \to \infty$. Hence for large values of α an asymptotic expansion of equation (2.16) must be used.

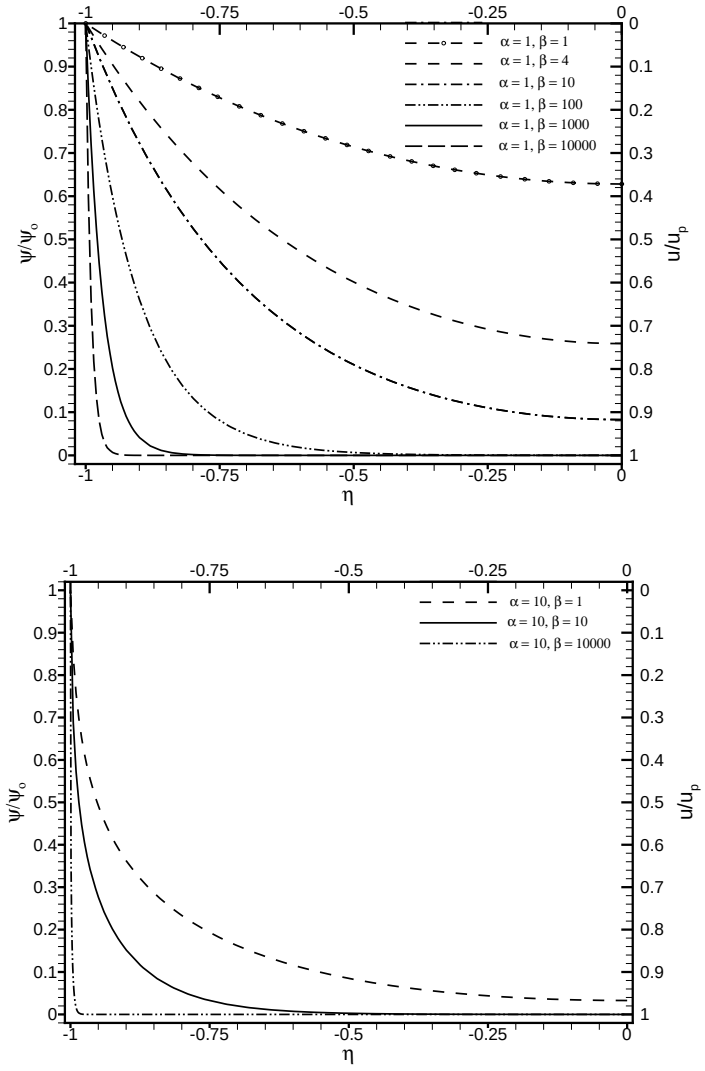

FIGURE 2. Variation of normalized electric charge potential ψ/ψ_o across the half of a channel for various values of α and β. The figures also show velocity profiles for pure electroosmotic flow given by equation (4.5).

2.1. *Near Wall Potential Distribution*

In this section, we present the potential distribution as a function of the near wall parameter $\zeta = y'\omega$, where $y' = h - y$ is the distance from the wall, and ω is the Debye-Hückel parameter given by (2.13). The results for $\alpha = 1, \beta \geqslant 100$ and for $\alpha = 10, \beta \geqslant 10$ correspond to sharp decay of the potential to zero in the channel center. This enables us to determine the near wall potential distribution without interactions of the two walls. Figure 3 presents the near wall potential distribution ψ^* as a function of ζ for several α and β values. It is observed from the figure that ψ^* is only a function of the ionic energy parameter α and is *independent of* β. This observation is very important in defining an *effective electric double layer thickness* δ^*. In other words, the potential distribution, for

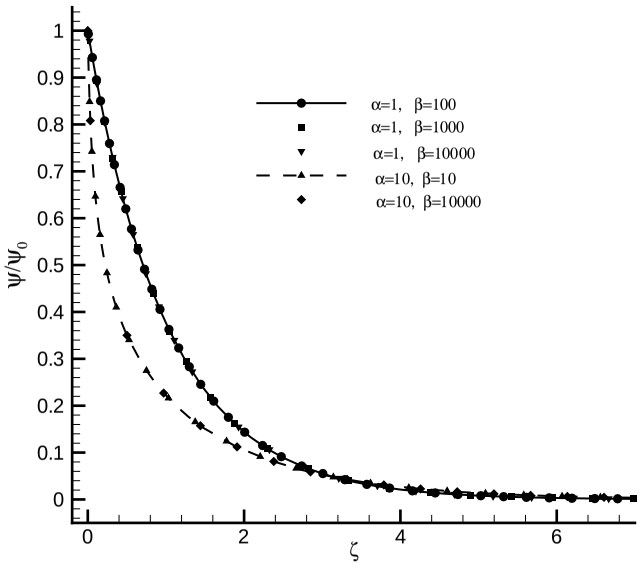

FIGURE 3. The potential distribution within the electric double layer as a function of the inner-layer scale ζ is *independent of* β.

a given channel dimension h and ionic energy parameter α, will decay to zero rapidly. Hence the effect of the EDL is present in a layer δ^* sufficiently close to the walls. Since, the EDL length based on the near wall parameter ζ is independent of β, we can write δ^* as:

$$\delta^* = \int_0^{\hat{\zeta}} \psi^* d\zeta. \tag{2.17}$$

where, $\hat{\zeta}$ is a large enough distance that includes variations in ψ^*; typically $\hat{\zeta} \simeq 10$. Since $\omega h = \sqrt{\alpha\beta}$, the near wall scaling parameter (ζ), and the nondimensional distance (η^*) can be represented in terms of each other (i.e. $\zeta = \sqrt{\alpha\beta}\eta^*$). Hence, one can obtain δ^* by integration of the numerical data or using equation (2.16) for various α values, and use it as an *effective EDL thickness* for evaluating its effect for various channel height and α values. Typical δ^* and α values are presented in table 1. In section §4 we will use δ^* to obtain relationships for the shear stress, velocity and pressure distributions for mixed electroosmotic/pressure driven channel flows.

Finally, substituting $\zeta = \sqrt{\alpha\beta}\eta^*$ in equation (2.16) we obtain

$$\psi^*(\zeta) = \frac{4}{\alpha} \tanh^{-1}\left[\tanh\left(\frac{\alpha}{4}\right)\exp\left(-\zeta\right)\right]. \tag{2.18}$$

This shows that the potential distribution within the electric double layer (EDL) is independent of β, and it is only a function of the ionic energy parameter α, when plotted as a function of the distance from the surface normalized by the Debye length.

α	1	5	10	15	20	25
δ^*	0.98635	0.75670	0.47731	0.32765	0.24657	0.19739
α	30	35	40	45	50	100
δ^*	0.16449	0.14099	0.12337	0.10966	0.09870	0.04935

TABLE 1. Variation of δ^* as a function of the ionic energy parameter α

3. Governing Equations

The electroosmotic flow is created by applying an effective electric field $\vec{E}_e$ in the streamwise direction, as shown in figure 1. The effective electric field can be represented as the gradient of an effective electric potential $\vec{E}_e = -\nabla\phi$. Then the total electric field $\vec{E}$ is obtained by summing $\vec{E}_e$ with the electric field due to the potential field ψ. Hence,

$$\vec{E} = -\nabla\Phi = -\nabla\psi - \nabla\phi. \tag{3.1}$$

This total electric field interacts with the electric charge distribution in the channel, and creates an electrokinetic body force on the fluid. The ionized incompressible fluid flow with electroosmotic body forces are governed by:

$$\rho_f(\frac{\partial\vec{V}}{\partial t} + (\vec{V}.\nabla)\vec{V}) = -\nabla P + \mu\nabla^2\vec{V} + \rho_e\vec{E}, \tag{3.2}$$

where P is the pressure field, and ρ_e and $\vec{E}$ are determined by equations (2.12) and (3.1), respectively. Due to incompressibility the conservation of mass is simply given by

$$\nabla.\vec{V} = 0. \tag{3.3}$$

The main simplifying assumptions and approximations in our analysis are:

(*a*) The fluid viscosity is *independent of the shear rate*. Hence, we assume a Newtonian fluid.

(*b*) The fluid viscosity is *independent of the local electric field strength*. This condition is an *approximation*. Since the ion concentration and the electric field strength within the EDL is increased, the viscosity of the fluid may be affected. However, such effects are neglected in our analysis which considers only dilute solutions.

(*c*) The Boltzmann-Poisson equation (2.12) is valid when the ion convection effects are negligible. Hence, our analysis is valid for Stokes flows, or for fully developed channel flows.

(*d*) The solvent is continuous and its permittivity is not affected by the overall and the local electric field strength.

(*e*) The ions are point charges.

(*f*) The only work done in bringing an ion from the bulk fluid up to a certain point, where the electric potential is ψ, is the electric work: $ze\psi$ (for the details see Hunter, 1981).

3.1. *Numerical Formulation and Validation*

We used a high order finite element method for solution of the Boltzmann-Poisson equation (2.12), and the incompressible Navier-Stokes equations given by (3.2 and 3.3). The numerical algorithm $\boldsymbol{\mathcal{N}\varepsilon\kappa\mathcal{T}\alpha r}$ employs *modal spectral expansions* in quadrilateral and

unstructured triangular meshes (Karniadakis & Sherwin, 1999). Hence we can discretize complex engineering geometries with great flexibility (due to the unstructured grid) and can still maintain the high-order numerical accuracy. The details for numerical discretizations used for the Navier-Stokes equations with arbitrary body forces are given in (Warburton, 1999).

Our specific contribution is the solution of the non-linear Boltzmann-Poisson equation given by (2.12). We used a Galerkin projection, and solved the weak variational form of equation (2.12). We utilized a Newton iteration strategy for a variable coefficient Helmholtz equation to treat the exponential non-linearity. Our iteration scheme is given as:

$$\left[\nabla^2 - \beta\cosh(\alpha\,(\psi^*)^n)\right](\psi^*)^{n+1} = \beta\sinh(\alpha\,(\psi^*)^n) - \beta\,(\psi^*)^n\cosh(\alpha\,(\psi^*)^n),$$

where n shows the iteration number. The electric potential solution of a previous iteration is used for evaluation of the non-linear forcing function, and the resulting system is solved until the residual is reduced beyond a certain level (typically 10^{-10}). The numerical solution of equation (2.12) is challenging due the *exponential non-linearity* associated with the hyperbolic-sine function. Especially for large values of α the non-linear forcing increases rapidly for any value of β, making the numerical solution challenging. For very large values of β with $\alpha = 1$, similar difficulties also exist. Accurate resolution of the EDL requires high grid density within the EDL. A typical mesh structure for the $\alpha = 1$ and $\beta = 10,000$ case is presented in figure 4 (right). The spectral element mesh has 22 elements across the channel width, spaced in biased fashion with minimum width of $0.001h$ very near the walls. Once the mesh topology is fixed, we vary the modal expansion order N to further resolve the problem. For rectangular elements shown in figure 4, $N = 2$ correspond to a quadratic solution in ψ^*, typically obtained by the finite-element schemes. In spectral element method the basic grid structure is fixed and successively higher values of N are used to further resolve the problem.

The total electric field and the body force on the fluid both depend on the gradients of the potential field ψ^*. Therefore, we used equation (2.15) directly to determine the numerical accuracy of our results. Hence the numerical solution of ψ^* and its η-direction derivative (i.e. $\partial\psi^*/\partial\eta$) are used at quadrature points, along with the calculated value of ψ_c^* using equation (2.15) to determine the numerical discretization errors. Variation of the numerical error as a function of the modal expansion order N is presented in figure 4 (left) for the mesh topology shown on the right figure. The L_∞ error is the maximum error in the domain, and L_2 error norm is defined as:

$$L_2 = \frac{\left[\int_\Omega R\left(\psi^*, \frac{\partial\psi^*}{\partial\eta}, \psi_c^*\right)^2 d\Omega\right]^{1/2}}{\int_\Omega d\Omega},$$

where Ω shows the entire flow domain, and R is the residual of equation (2.15) given by:

$$R\left(\psi^N, \frac{\partial\psi^N}{\partial\eta}, \psi_c^N\right) = \frac{d\psi^N(\eta)}{d\eta} - (\frac{\omega h}{\alpha})\left[2cosh(\alpha\psi^N) - 2cosh(\alpha\psi_c^N)\right]^{\frac{1}{2}}, \qquad (3.4)$$

where the superscript N shows the numerical results. Here we must emphasize that the residual R in the L_2 error norm is usually defined as the difference between the numerical and the analytical values of a parameter. However, in our case we used equation (2.15), which relates the values of the potential ψ^* and its directional derivatives. Hence the L_2 error norm presented in figure 4 corresponds to *a form of* H_1 error norm. The convergence results presented in figure 4 show *exponential decay of the discretization*

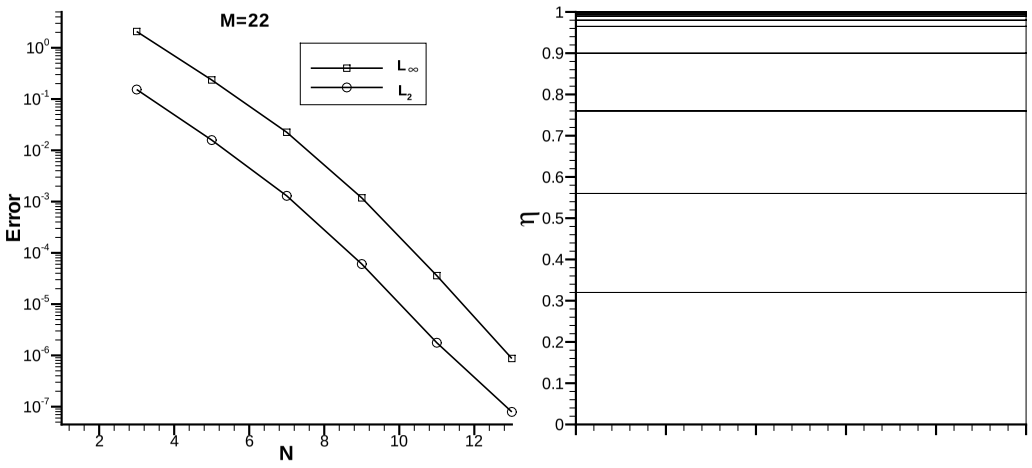

FIGURE 4. On the left Spectral convergence in L_2 and L_∞ norms as a function of the spectral expansion order N. On the right: The elemental structure of the grid in the upper half of the channel. There are a total of 22 elements across the channel, and each element is discretized with N^{th} order modal expansion per direction. The quadrature points for this modal expansion is not shown for the clarity of the figure. The convergence results are for the case $\alpha = 1$ and $\beta = 10,000$.

error with increased N, typical of the spectral element methodology. This high resolution capacity enables us to accurately resolve the electric double layers with relatively less number of elements compared to the low-order finite element schemes.

4. Analysis for Channel Flows

In this section we analyze the mixed electroosmotic/pressure driven flows in micro-channels. We assume that the channel height h is much smaller than the channel width w (i.e. $h << w$). Hence, the flow can be treated as two-dimensional as shown in figure 1. We also assume fully developed, steady flow with no-slip boundary conditions.

4.1. *Streamwise Momentum Equation*

The streamwise momentum equation is given by:

$$\frac{\partial P}{\partial x} = \mu \frac{\partial^2 u}{\partial y^2} - \rho_e Y_e, \tag{4.1}$$

where u is the streamwise velocity. For convenience E_x is replaced by $-Y_e$, where $||Y_e||$ is the net electric field in the streamwise direction. The Y_e includes the imposed electric field $d\phi/dx$. In the case of pressure driven flows, Y_e also includes the electric field due to the *streaming potential* (see §6 for detailed explanation of the streaming potential). Due to the simple geometry $\frac{\partial \psi}{\partial x} = 0$, the ψ field does not contribute to Y_e. Although the presence of the streaming potential field can complicate the analysis, let us assume for the time being that $||Y_e||$ is a given net streamwise electric field. Using this and equation (2.14) for ρ_e we obtain

$$\frac{\partial P}{\partial x} = \mu \frac{\partial^2 u}{\partial y^2} + \frac{DY_e}{4\pi} \frac{d^2 \psi}{dy^2}. \tag{4.2}$$

In the absence of the pressure gradients, balance between the viscous diffusion terms and the electroosmotic forces result in the Helmholtz-Smoluchowski electroosmotic velocity u_p (Probstein, 1994):

$$u_p = MY_e = \psi_o DY_e/4\pi\mu = \frac{\psi_o \epsilon Y_e}{\mu} \tag{4.3}$$

where, M is the mobility ($M = \psi_o D/4\pi\mu$). We non-dimensionalize equation (4.2), and present the non-dimensional streamwise momentum equation:

$$\frac{\partial P^*}{\partial \xi} = \frac{\partial^2 U}{\partial \eta^2} + \frac{d^2\psi^*}{d\eta^2}, \tag{4.4}$$

where, $U = \frac{u}{u_p}$, and $P^* = \frac{P}{\mu u_p/h}$, and $\xi = x/h$. Since we are analyzing Stokes flow, the pressure is normalized by the viscous forces, rather than the dynamic head.

In the case of zero net pressure gradient one can easily integrate equation (4.4) to obtain

$$U(\eta) = 1 - \psi^*(\eta). \tag{4.5}$$

In the limit of small Debye lengths (for $\alpha \geqslant 1$ and $\beta \geqslant 100$) the potential decays very fast within the thin electric double layer and a uniform "plug-like" velocity profile is obtained in most of the channel. The plug flow behavior have been observed in various experiments and reported earlier by Molho *et al.*(1998). In figure 2 we present the theoretical velocity profiles obtained for various values of α and β. For $\alpha = 1$ and $\beta < 100$ the velocity gradually increases across the channel from zero on the wall to a value less than u_p. However for $\beta \geqslant 100$ the velocity distribution resembles the "plug like" velocity. Formation of this "uniform velocity" in the bulk of the channel is utilized to derive analytical solutions.

For the mixed electroosmotic/pressure driven flows we can use the linearity of the Stokes equations and decompose our velocity field into two parts:

$$U = U_{Pois} + U_{EO},$$

where U_{Pois} corresponds to the pressure driven channel flow velocity (i.e. plane Poiseuille flow), and U_{EO} is the electroosmotic flow velocity given by (4.5). Following Burgreen and Nakache (1964) we obtain the following non-dimensional velocity profile.

$$U(\eta) = -\frac{1}{2}\frac{dP^*}{d\xi}\left(1-\eta^2\right) + 1 - \psi^*(\eta), \tag{4.6}$$

where $\frac{dP^*}{d\xi}$ corresponds to the pressure gradient in the mixed electroosmotic/pressure driven flow regime. We can substitute the solution for ψ^* from equation (2.16) to obtain an analytical formula for the velocity distribution. However, we must keep in mind that (2.16) is valid when $\psi_c^* = 0$, hence it is an approximation.

Integrating the velocity distribution across the channel we obtain the normalized volumetric flowrate (by $u_p h$) per unit width of the channel

$$\dot{Q} = -\frac{2}{3}\frac{dP^*}{d\xi} + 2(1 - \frac{\delta^*}{\sqrt{\alpha\beta}}), \tag{4.7}$$

where we integrated the ψ^* term in equation (4.6) using equation (2.17) in the following form:

$$\int_{-1}^{1} \psi^* d\eta = 2\int_0^1 \psi^* d\eta = \frac{2}{\sqrt{\alpha\beta}}\int_0^{\hat{\zeta}} \psi^* d\zeta = \frac{2\delta^*}{\sqrt{\alpha\beta}}.$$

For most of the micro-fluidic experiments a certain amount of pressure drop along the

channel is applied, and the resulting volumetric flowrate is measured. Equation (4.7) shows that the volumetric flowrate in micro-channels can be manipulated using the electroosmotic effects.

Also for specified volumetric flowrate, one can obtain the pressure gradient along the channel. This enables us to investigate the mixed electroosmotic/pressure driven flow regime. In the next section, we will present simulation results for an *electroosmotically driven pump*. For the specified flowrate case, we can calculate the resulting pressure gradient as:

$$\frac{dP^*}{d\xi} = 3\left(1 - \frac{\delta^*}{\sqrt{\alpha\beta}}\right) - \frac{3}{2}\dot{Q}. \tag{4.8}$$

We find the shear stress on the wall for the mixed pressure/electroosmotically driven flow region by differentiating (4.6) with respective to η, and utilizing equation (2.15). The result is:

$$\tau_w^* = \sqrt{\frac{\beta}{\alpha}}\sqrt{2cosh(\alpha) - 2cosh(\alpha\psi_c)} - \frac{dP^*}{d\xi}. \tag{4.9}$$

This is an implicit *exact* relation under the assumptions of our analysis, which require ψ_c^*. Assuming that the $\psi_c^* = 0$ (valid for $\alpha \geqslant 1$ and $\beta > 100$) we find an approximate relation:

$$\tau_w^* = \sqrt{\frac{\beta}{\alpha}}\sqrt{2cosh(\alpha) - 2} - \frac{dP^*}{d\xi}. \tag{4.10}$$

The first term on the right hand side is due the variation of velocity within the electric double layer, and the second term is due to the pressure driven velocity profile.

4.2. *Cross-Flow Momentum Equation*

The cross-flow velocity v vanishes due to the fully developed, incompressible flow with no-penetration boundary condition on the walls. Therefore the cross-flow momentum equation predicts a balance between the electrokinetic forces and pressure in the cross-flow direction.

$$\frac{\partial P}{\partial y} = -\rho_e \frac{d\psi}{dy}. \tag{4.11}$$

After substituting $\rho_e = -\frac{D}{4\pi}\frac{d^2\psi}{dy^2}$, and rearranging the $\frac{d\psi}{dy}(\frac{d^2\psi}{dy^2})$ terms, we write the cross-flow momentum equation in the following non-dimensional form:

$$\frac{\partial P^*}{\partial \eta} = \frac{\psi_o}{2hY_e}\frac{d(\frac{d\psi}{d\eta})^2}{d\eta}. \tag{4.12}$$

Equation (4.12) can be partially integrated across the channel (in η), resulting in

$$P^*(\xi,\eta) = \frac{\psi_o}{2hY_e}(\frac{d\psi^*}{d\eta})^2 + c(\xi) \tag{4.13}$$

where, $c(\xi)$ is due to the pressure variation along the channel. However, using equation (4.8) we can find the form for $c(\xi)$, and we can substitute for $\left(\frac{\partial\psi^*}{\partial\eta}\right)^2$ using equation (2.15). This results in an *analytical relation for the pressure distribution in the entire channel*

$$P^*(\xi,\eta) = P_{in}^* + \frac{\beta\psi_o}{\alpha hY_e}\left[cosh(\alpha\psi^*) - cosh(\alpha\psi_c^*)\right] + \left[3(1 - \frac{\delta^*}{\sqrt{\alpha\beta}}) - \frac{3}{2}\dot{Q}\right]\xi, \tag{4.14}$$

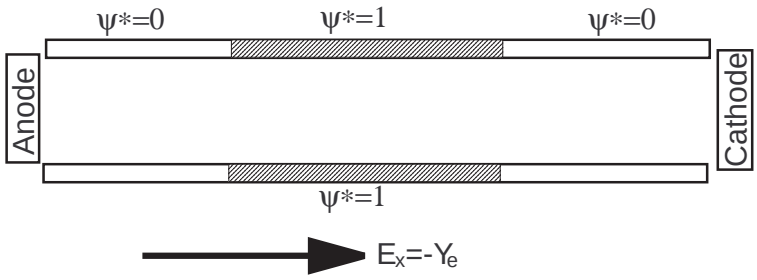

FIGURE 5. Schematic view of mixed electroosmotic/pressure driven flow channel. The inlet and the exit portions of the channel has negligible electroosmotic effects.

where P^*_{in} is the center line pressure at the channel inlet. This equation shows large variations of pressure in the *cross-flow direction* due to the hyperbolic cosine terms. For $\alpha \geqslant 1$ and $\beta \geqslant 100$ we can predict the difference in the wall and channel center pressure at a given ξ location as:

$$P^*_{wall} - P^*_{center} = \frac{\beta \psi_o}{\alpha h Y_e} \left[cosh(\alpha \psi^*) - 1 \right]. \tag{4.15}$$

This shows *large differences* between the channel center and the wall pressure for increased values of α. We must note here that $\psi_o / Y_e h$ is the electric field across the channel normalized with the effective streamwise electric field Y_e. The magnitude of the cross flow pressure variation depends on this ratio, and can be easily calculated by the experimental conditions. In the next section, in figure 9 and table 3 we will present the comparison of the numerical and analytical predictions.

5. Numerical Results

Let us consider a specific case of a channel made out of two different materials. The first material exhibit negligible electroosmotic effects, and it is used at the entry and the exit portions of the channel. The second material, on the other hand exhibits strong electroosmotic effects, and it is used for the middle section of the channel. This configuration is shown in figure 5. It may be possible to fabricate such a micro-channel by using different materials (conductors and insulators) on various portions of the channel surface. In practice, it is also possible to obtain variations in the wall potential due to the contamination in the capillary walls, variations in the wall coating, or gradients in the buffer *pH* (Molho *et al.*, 1998). Therefore the proposed configuration has some practical relevance, and it is an *excellent test-bed* to study mixed electroosmotic/pressure driven flows.

In our simulations, we specified the volumetric flowrate at the channel entrance, and calculated the corresponding velocity and pressure distribution in the rest of the channel by numerical solution of equations (2.12), (3.2), and (3.3). In order to eliminate the channel entry effects, we specified fully developed (parabolic) velocity profile at the inlet with a maximum inlet velocity of u_{in}. We present our numerical simulation results as a function of the ratio of the specified inlet velocity u_{in} to the Helmholtz-Smoluchowski electroosmotic velocity u_p. Using this non-dimensional ratio $U_{in} = u_{in}/u_p$ (here $\dot{Q} = 4/3U_{in}$) we can generate various levels of pressure gradients in the mixed electroosmotic/pressure driven zone. The numerical simulations are performed for $Re = 0.005$ flow, where the Re is based on the average channel velocity and the channel half height. We kept the stream-

$U_{in} = \frac{u_{in}}{u_P}$	$dP^*_{num}/d\xi$	$dP^*_{ana}/d\xi$	$\tau_{w(num)}$	$\tau_{w(ana)}$
2.500	-2.0268	-2.0296	106.334	106.249
2.000	-1.0284	-1.0296	105.334	105.249
1.485	0.0000	0.0000	104.301	104.219
1.000	0.9734	0.9704	103.334	103.249
0.500	1.9676	1.9704	102.334	102.249

TABLE 2. The numerical and analytical estimates of the pressure gradient (4.8) and wall shear stress (4.9) in the mixed electroosmotic-pressure driven flow regime. Differences between the numerical results and the analytical formulas are less than 1% for a $7^{th}-$order spectral element discretization for $\alpha = 1, \beta = 10,000$ case. The numerical error is consistent with the convergence results shown in figure 4.

wise electric field strength and the EDL properties constant at $\alpha = 1$ (corresponding to $\psi_o = 24mV$) and $\beta = 10,000$. Therefore, the Debye length in the simulations is about $1/100^{th}$ of the channel half height, and we resolve the entire flow domain including the EDL.

In figure 6 we present the non-dimensional pressure distribution along the channels for various values of U_{in}. Here the pressure is normalized with $\mu u_p/h$, consistent with the Stokes flow non-dimensionalization. The numerical algorithm specifies zero gauge pressure at the channel outflow. Hence, all of the numerical results show zero gauge pressure at the exit. The entry and the exit portions of the channels are pure pressure driven, and the electroosmotic forces are present only at $3.1 \leqslant \xi \leqslant 6.2$. The effective electric field is in the positive streamwise direction. Figure 6 shows variation of channel center-line pressure as a function of various U_{in} values. Using equation (4.8) we can estimate the theoretical value of U_{in} that results in a desired pressure gradient in the mixed region. For example, the theoretical value of $U_{in} = 1.485$ for $\alpha = 1$ and $\beta = 10,000$ gives zero pressure gradient in the mixed electroosmotic-pressure driven flow region. The analytical and numerical predictions of the pressure gradients at this mixed region are presented in table 2 for various values of U_{in}. The theoretical and numerical predictions agree within 1%, consistent with the convergence results shown in figure 4.

The corresponding velocity profiles across the channel at $\xi = 4.5$ are presented in figure 7. Pure "plug-like velocity" profile is observed for $U_{in} = 1.485$, as predicted by the theory. The velocity profiles for favorable and adverse pressure gradient flows are also presented in figure 7. For example, $U_{in} = 2.5$ corresponds to a favorable pressure gradient case, which is a combination of a plug-like flow with a parabola in the bulk of the channel. The corresponding pressure variation shown in figure 6 indicates sharp pressure drops at the entry and the exit portions of the channel. However, in the mixed zone, the pressure drop is relatively low due to the electroosmotic pumping.

The adverse pressure gradient case of $U_{in} = 0.5$ is an *electrokinetically driven micro-pump*. For this case, the inlet and the exit pressures are the same, corresponding to a biological/chemical detection and analysis laboratory on a chip device that is exposed to atmospheric pressure. The entire flow is driven by the electrokinetic forces, which overcomes the drag within the entire channel system. The pressure drops at the inlet and exit portions of the channel ($\xi \leqslant 3.1$ and $\xi \geqslant 6.2$) are due to the shear stress. A micro-pump must be able to raise the system pressure to be able to drive the flow. The electroosmotic pump is doing precisely this. The net pressure gradient is positive within the pump, as shown in figure 6. Here we must note that in a pure electroosmotic

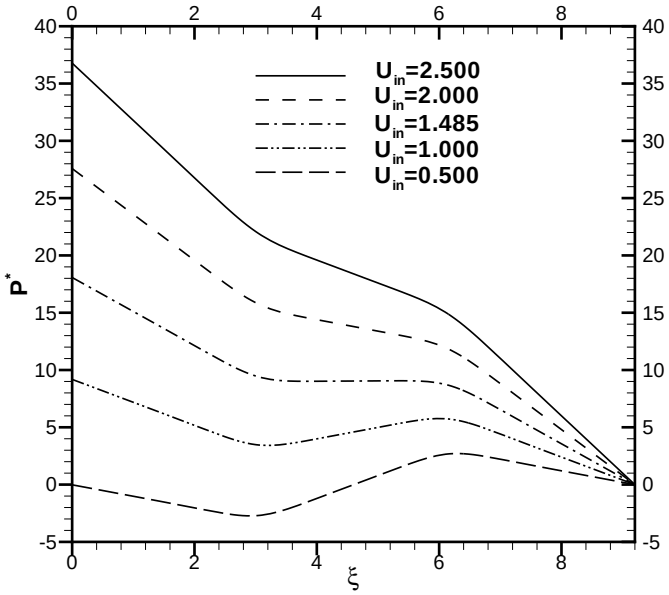

FIGURE 6. The normalized pressure distribution in a mixed electroosmotic/pressure driven channel for various values of U_{in}. The $U_{in} = 1.485$ correspond to "plug-like flow". The electroosmotic forces are present only at $3.1 \leqslant \xi \leqslant 6.2$. Here, $\alpha = 1$, and $\beta = 10,000$.

system, the plug-like velocity profiles with zero-pressure gradient will be obtained. In the case of $U_{in} = 0.5$, adverse pressure gradient is present to overcome the pressure drop at the inlet and the exit sections. Hence, any mixed flow system should exhibit a similar behavior to our simulation results presented in figure 6. The velocity profile for this case shown in figure 7 indicates combination of plug and adverse pressure gradient channel flow behavior. The net volumetric flowrate is positive, as can be seen from figure 7.

The shear stress in the mixed electroosmotic/pressure driven flow region is enhanced due to the presence of the EDL and the pressure gradients. Comparisons of shear stress estimates obtained by the numerical simulations and the analytical equation (4.9) are also presented in table 2. The error in the numerical results are about 0.08 percent.

For a closed system it is possible to create very large pressures using the electroosmotic forces. This can be used for micro-scale actuation of micro-pistons or micro-bellow mechanisms. We simulated such a configuration by closing the exit of our channel. Of course zero net flow rate is imposed at the channel inlet. Due to the presence of the electroosmotic forces the pressure raises linearly within the electroosmotic region, as shown in figure 8. This pressure raise is accompanied by electroosmotic flow near the channel walls along the electric field (see velocity profiles in figure 8), and a reverse flow in the middle of the micro-channel.

We have shown in the previous section that there are significant variations in pressure within the EDL. We demonstrate this trend in figure 9 by presenting our numerical simulation results at $\xi = 4.5$. In analyzing figure 9 one should notice the sharp variation in pressure across the EDL, especially the difference in the pressure between the wall and the center line. Since we present the gauge pressure with respect to the channel outlet, the relative magnitude of pressure at the channel center is irrelevant. For our

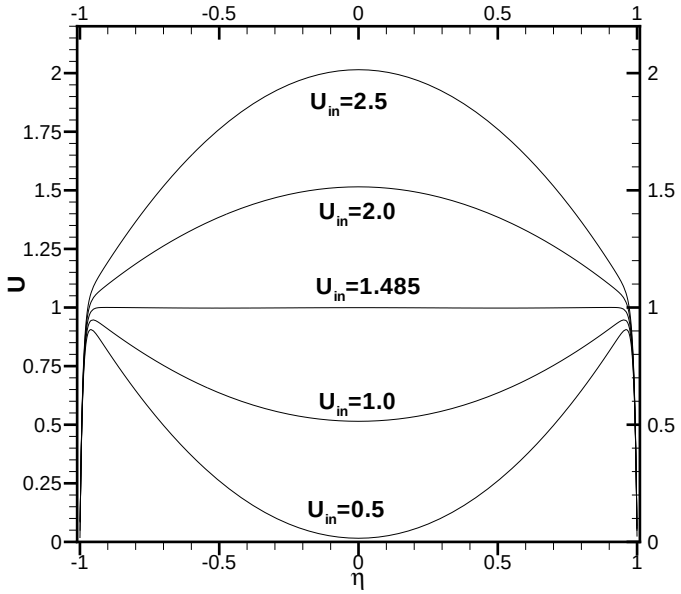

FIGURE 7. The velocity distribution in a mixed electroosmotic/pressure driven channel for various values of U_{in}. The $U_{in} = 1.485$ correspond to "plug-like flow". For larger and smaller values of U_{in} favorable and adverse pressure gradients are obtained, respectively. Here, $\alpha = 1$, and $\beta = 10,000$.

U_{in}	$\lvert P^*_{wall} - P^*_{center}$
0.500	34.4890
1.000	34.4891
1.485	34.4891
2.000	34.4890
2.500	34.4890

TABLE 3. The numerical estimates of the pressure difference between the wall and the centerline in the mixed electroosmotic/pressure driven flow regime. Analytical value predicted from equation (4.15)is 34.505. The results presented in this table are obtained for $\alpha = 1, \beta = 10,000$.

simulation conditions the pressure jump across the EDL is predicted by equation (4.15) to be 34.505. The theory also indicates that the pressure increase is independent of the streamwise pressure gradient. The pressure jump across the EDL obtained from our numerical results, presented in table 3, also confirms this finding.

5.1. *Electroosmotic Slip Velocity*

The electroosmotic forces are concentrated within the EDL, which has a thickness in the order of 100 nm to $1nm$. On the other hand, the micro-channels utilized for many laboratory on a chip applications have a typical height of $100\mu m$ to $1\mu m$. This two- to three- orders of magnitude difference in the EDL and the channel length scales is a great difficulty in numerical simulation of electroosmotically driven micro-flows. Therefore, it

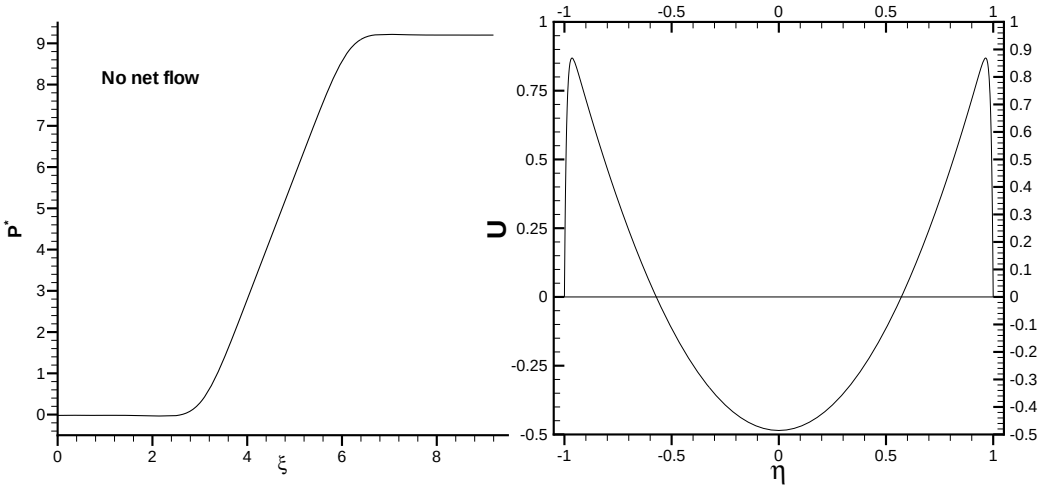

FIGURE 8. Pressure buildup along the micro-channel for zero net flowrate (on the left). The velocity distribution across the channel for the zero flowrate case (on the right).

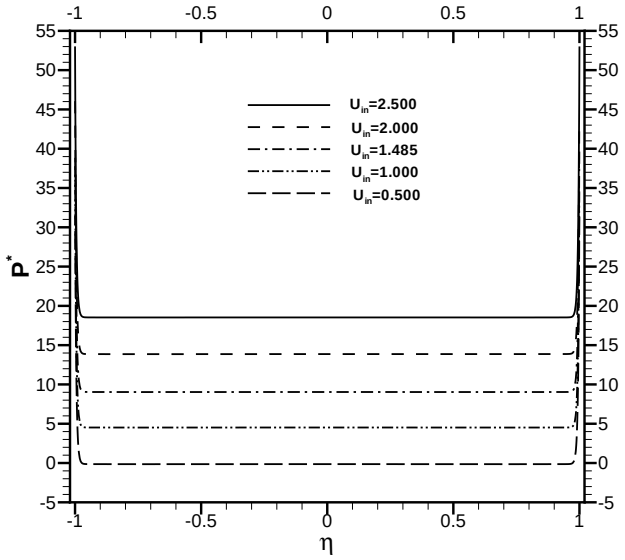

FIGURE 9. The pressure distribution across the micro-channel at $\xi = 4.5$. The pressure suddenly increases within the EDL. This increase is independent of the streamwise pressure gradient as shown by equation (4.15). In this simulation $\alpha = 1.0$ and $\beta = 10,000$.

may be very effective to develop a *unified slip condition* that incorporates the EDL effects in analysis and simulation. The velocity profiles in figure 7 show presence of sharply varying layers within a few Debye length λ. This distance is about 4λ as seen in figure 3.

The presence of the EDL resembles the Knudsen layers in rarefied gas dynamics, where there is a sub-layer between the boundary layer and the wall, which has a thickness of a few gas mean free path. In the slip flow regime, the Knudsen layer is confined to about

$1 \sim 10\%$ of the boundary layer thickness, and its effects on gas flow is implemented by a *slip boundary condition* (for details see Beskok & Karniadakis, 1999).

We analyzed the electroosmotic slip velocity by postulating a generalized slip condition in the following form:

$$U_f - U_w = A(\frac{\lambda}{h})\frac{\partial U}{\partial \eta}|_w + B,$$

where, A and B are constants, and $\lambda/h = 1/\sqrt{\alpha\beta}$ is the Debye length normalized with the channel half height. U_f is the fluid slip velocity on the wall, and U_w is the wall velocity. The constant A is a correction factor for the effective EDL thickness in the above equation. The term $\frac{\partial U}{\partial \eta}$ is evaluated on the wall using the outer flow, neglecting the EDL and it is proportional to the shear stress due to the outer flow. The constant B corresponds to a constant slip velocity, independent of the pressure gradient. Based on this boundary condition, the analytic solution of velocity for a pressure driven channel flow is

$$U(\eta) = -\frac{1}{2}\frac{dP^*}{d\xi}\left(1 + \frac{2A}{\sqrt{\alpha\beta}} - \eta^2\right) + B, \tag{5.1}$$

Comparison of this result with the analytical solution given by equation (4.6) indicates that $A = 0$. Hence, the electroosmotic slip is not a function of $\frac{\partial U}{\partial \eta}$, but it is a constant. The value of B can be found by comparison of (5.1) with the analytical solution (4.6), and (by ignoring the EDL effects) $B = 1$. Hence, in dimensional form the electroosmotic slip velocity is the Helmholtz-Smoluchowski velocity u_p, given by equation (4.3).

If one assumes a constant slip $B = 1$, the volumetric flowrate will be *overpredicted* due to the velocity distribution within the EDL. However, we can correct this flowrate value by using equation (4.7). The correction to the flowrate will be based on the function $\delta^*/\sqrt{\alpha\beta}$. Using table 1 and the values of α and β for a given channel, we can find the correction to the flowrate. Once the flowrate is known we can calculate the correct pressure gradient $\frac{\partial P^*}{\partial \eta}$. The parabolic velocity distribution obtained with this correct pressure gradient and utilization of the electroosmotic slip velocity U_p is shown in figure 10. The figure also shows the near wall velocity distribution within the 10% of the channel half height. Clearly the electroosmotic slip velocity is equivalent to U_p, and it is independent of the local pressure gradient or *the vorticity of the bulk flow*. This is at least the case for channel flows.

Once we verified that the appropriate slip velocity is U_p, we investigated the ways of imposing this slip velocity on the walls, and hence not modeling the flow within EDL. However, without apriory knowledge of the effect of the EDL on the flow field, one can not obtain the correct pressure gradient or the flow rate. The error we make in conservation of mass by neglecting the velocity distribution within the EDL is $2\delta^*/\sqrt{\alpha\beta}$. For engineering applications with $\alpha = 1$ and $\beta = 10,000$, the error in using the electroosmotic slip velocity is about 2% in conservation of mass.

In regards to the errors in the momentum equation, neglecting the shear stresses due to the velocity distribution within the EDL will be in gross error. The shear stress for the analytical solution is given by equation (4.10). However, the total drag force can always be predicted using a control volume approach for the entire channel and imposing Newton's second law. Therefore, numerical models which use U_p as the wall slip velocity, and do not necessarily resolve the flow within the EDL can be used for many engineering applications. However, the limitations of this approach must always be considered carefully.

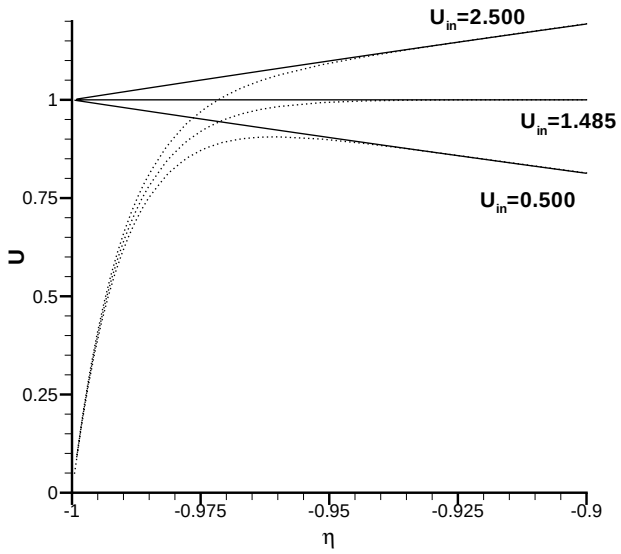

FIGURE 10. A magnified view of the velocity distribution near the wall for $\alpha = 1$ and $\beta = 10,000$. Extrapolation of the velocity using a parabolic velocity profile with constant slip value U_p are shown by the solid lines. The numerical solution of velocity distribution within the EDL is shown by the dashed lines.

6. Streaming Potential Effects

In the *absence of an applied electric field*, a polar medium forced to move in a capillary by an external pressure gradient, experiences an electric field in the opposite direction to the flow. This is known as the *streaming potential*. The detailed analysis of the streaming potential effects are presented in two influential manuscripts by Burgreen & Nakache (1964) and Yang *et al.*(1998).

In this paper, we studied mixed electroosmotic/pressure driven flows by using an *effective* electric field $-Y_e$. However, in experiments a known electric field $-Y_o$ is imposed along the channel. If pressure driven flow is generated, there will be streaming potential effects, and the imposed electric field and the effective electric field will differ. In this section, we will present formulas to incorporate the streaming potential effects into the calculation of $-Y_e$. Therefore, the experimental data can be properly interpreted.

Burgreen & Nakache have considered a basic electrokinetic circuit (see Figure 7 in Burgreen & Nakache, 1964), which includes an externally imposed electric field $-Y_o$ and an external resistance of R_o. The fluid has electric conductivity of K_o, and the microchannel is assumed to have length L, width W and height h. Based on these conditions the following relationship between the *effective electric field* Y_e and the *imposed electric field* Y_o is obtained (for details on the derivation see Burgreen & Nakache, 1964):

$$Y_e = \frac{Y_o - \frac{R_o}{L}\hat{B}}{1 + \frac{R_o K_o W h}{L} + R_o \hat{A}}. \tag{6.1}$$

Here $\hat{B}$ is a coefficient with units of current, and it is given by

$$\hat{B} = MW\frac{\partial P}{\partial x}(2 + \frac{I_1}{\sqrt{\beta}}), \quad \text{where}$$

α	I_1	I_2
1	1.9727	0.51
5	0.6768	4.11
10	0.3019	29.28
15	0.1692	240.81
20	0.1103	2202.45

TABLE 4. Values of the streaming potential integrals I_1 and I_2 as a function of α.

$$I_1 = -\frac{1}{\alpha^{3/2}} \int_0^{\hat{\zeta}} \sinh(\alpha\psi^*)\zeta^2 d\zeta.$$

The coefficient $\hat{A}$ has the units of ohm^{-1} and it is given by

$$\hat{A} = -\frac{2\epsilon\psi_o MW}{h^2}\sqrt{\frac{\beta}{\alpha}}\, I_2, \quad \text{where}$$

$$I_2 = \int_0^{\hat{\zeta}} \sinh(\alpha\psi^*)(1-\psi^*)d\zeta.$$

The integrals I_1 and I_2 are *independent of* β when evaluated in the near-wall coordinates ζ. Due to the sharp decay of the electric potential ψ^* within a few Dedye-Hückel parameter (ω) for $\alpha \geqslant 1$ and $\beta \geqslant 100$ the contributions to the above integrals diminish for values of $\zeta \geqslant 25$. For this reason we evaluated the above integrals up to $\hat{\zeta} = 25$ using the analytical solution for ψ^* given by equation (2.16). The values of these integrals are presented in table 4 as a function of α.

Equation (6.1) has two distinct limits. The first one is obtained when the external resistance $R_o = 0$. Under this condition we get $Y_e = Y_o$. The second limit is $R_o \to \infty$, which can also be interpreted as no external electric field Y_o is being imposed. The resulting electric field creates an electroosmotic flow towards the upstream, opposing the pressure driven flow. This effect can be used to explain the seminal micro-scale liquid flow results of Pfahler *et al.*(1991), where significant deviations from the regular Poiseuille flow results were reported.

7. Summary and Conclusions

In this paper we presented analytical and numerical analysis of mixed electroosmotic/pressure driven micro-channel flows. In particular, we have shown that the potential distribution within the electric double layer (EDL) is independent of β, and it is a function of the ionic energy parameter α only, when plotted as a function of the distance from the surface, normalized by the Debye length. This observation enabled us to define an effective EDL thickness, which is used in characterization of the mass flowrate defect due to the EDL. We derived analytical formulas for the flowrate, pressure gradient and shear stress in mixed electroosmotic/pressure driven flow conditions. We demonstrated the electroosmotic pumping concepts, which can be effectively used in design of micro-pumps with non-moving components. The analysis of cross-flow momentum equation enabled us to discover large pressure increase across the EDL, which might have been overlooked in previous research. Finally, we investigated utilization of the Helmholtz-Smoluchowski electroosmotic slip velocity in numerical simulation efforts.

We have shown that, although the mass flowrate predictions will have negligible errors, such slip-based models will significantly *under-predict* the wall shear stress.

In regards to the numerical simulation effort, we demonstrated spectral accuracy of our numerical results by formal convergence analysis and comparisons against the analytical results. This newly developed algorithm will be used to analyze the electrokinetically driven flows in complex micro-geometries in our future studies.

8. Acknowledgments

We would like to thank Dr. Haralambos Marmanis of Sofiatech and Dr. Ross Larsen of University of California at Santa Barbara for their valuable suggestions during the course of this study. AB would like to acknowledge the partial financial support provided by Texas High Education Council, Advanced Projects Program grant 000512-0418-1999, TW thanks DARPA F49620-96-1-0426 and DOE DE-FG02-98ER25346 for their support.

REFERENCES

Adamson, A. W. 1990 Physical chemistry of surfaces. fifth edition, Wiley Interscience Publication, New York.

Beskok, A. & Karniadakis, G. E. 1999 A model for flows in channels, pipes and ducts at micro and nano scales. *J. Microscale Thermophysical Engng* **3(1)**, 43–77.

Beskok, A., Trimmer, W. & Karniadakis, G. E. 1996 Rarefaction and compressibilty effects in gas micro flows. *J. Fluid Engng* **118**, 448–456.

Burgreen, D. & Nakache, F. R. 1964 Eletrokinetic flow in ultrafine capillary silts. *J. Phys. Chem.* **68(5)**, 1084–1091.

Cummings, E. B., Griffiths, S. K. & Nilson, R. H. 1999 Irrotationality of uniform electroosmosis. *Proc. SPIE Microfluidic devices and systems II* **3877**, 180–189.

Dahm, W. J. A., Diez-Gariez, F. J. & Paul, P. H. 2000 Microactuator array for sublayer control in turbulent boundary layers using the electrokinetic principles. *Proc. of AIAA aerospace Sciences Meeting* **2000-0548**, 1–18.

Ermakov, S. V., Jacobson, S. C. & Ramsey, J. M. 1998 Computer simulations of electrokinetic transport in microfabricated channel structures. *Anal. Chem.* **70**, 4494–4504.

Feynman, R.P., Leighton, R.B. & Sands, M. 1977 The Feynman Lectures on Physics, Volume II. Addison-Wesley, Massachusetts.

Gabriel K., Javris J. & Trimmer W. 1988 Small machines, large opportunities. *NSF Report.*

Gad-el-Hak M. 1999 The Fluid Mechanics of Microdevices-The Freeman Scholar Lecture. *Journal of Fluids Engineering*, **121**, 5–33.

Herr, A. E., Molho, J. I., Santiago, J. G., Mungal, M. G., Kenny, T. W. & Garguilo, M. G. 2000 Electroosmotic capillary flow with nonuniform Zeta Potential. *Anal. Chem.* **72**, 1053–1057.

Ho C.M. & Tai Y.C. 1998 Micro-electro-mechanical-systems (MEMS) and fluid flows. *Annual Review of Fluid Mechanics* **30**, 579–612.

Hunter, R. J. 1981 Zeta Potential in Colloid Science: Principles and Applications, first edition, Academic Press Inc, New York.

Jacobson, S. C., McKnight, T. E. & Ramsey, J. M. 1999 Microfluidic devices for electrokinetically driven parallel and serial mixing. *Anal. Chem.* **71**, 4455–4459.

Karniadakis G.E. & Sherwin S.J. 1999 Spectral/*HP* Element Methods for CFD, first edition, Oxford University Press.

Keh, H. J. & Liu, Y. C. 1995 Electrokinetic flow in a circular capillary with a surface charge layer. *J. Colloid and Interface Surfaces* **172**, 222–229.

Lyklema, J., Rovillard, S. & Coninck, J. D. 1998 Electrokinetics: The properties of the stagnant layer unraveled. *The ACS J. Surfaces and Colloids* **14(20)**, 5659–5663.

Molho, J. M., Herr, A. E., Desphande, M., Gilbert, J. R., Garguilo, M. G., Paul, P. H., John, P.M., Woudenberg, T. M. & Connel, C. 1998 Fluid tranport mechanisms in micro fluidic devices. *Proc. ASME Micro-Electro-Mechanical-Systems (MEMS)* **66**, 69–76.

PATANKAR, N. A. & HU, H. H. 1998 Numerical simulation of electroosmotic flow. *Anal. Chem.* **70**, 1870–1881.

PAUL, P. H., GRAGUILO, M. G. & RAKESTRAW, D. J. 1994 Imaging of pressure and electrokinetically driven flows through open capillaries. *Anal. Chem.* **70**, 2459–2467.

PFAHLER J., HARLEY J., BAU H. & ZEMEL J. 1991 Gas and liquid flow in small channels. *Proc. of ASME Winter Annual Meeting (DSC)* **32**, 49–59.

POLSON, N. A. & HAYES, M. A. 2000 Electroosmotic flow control of fluids on a capillary electrophoresis microdevice using an applied external voltage. *Anal. Chem.* **72**, 1088–1092.

PROBSTEIN, R. F. 1994 Physiochemical Hydrodynamics, second edition, Wiley and Sons inc., New York.

RICE, C. L. & WHITEHEAD, R. 1965 Electrokinetic flow in a narrow cylindrical capillary. *J. Phys. Chem.* **69**, 4017–4023.

WARBURTON, T. C. 1999 Spectral/hp methods on polymorphic multi-domains: algorithms and applications. PhD thesis, Brown University, Providence.

WILDING P., PFAHLER J., BAU H. H., ZEMEL J. N., & KRICKA L. J. 1994 Manipulation and flow of biological fluids in straight channels micromachined in silicon. *Clinical Chemistry* **40(1)**, 43–47.

YANG, C. & LI, D. 1998 Analysis of electrokinetic effects on the liquid flow in rectangular microchannels. *J. Colloids and Surfaces* **143**, 339–353.

YANG, C., LI, D. & MASLIYAH, J. H. 1998 Modeling forced liquid convection in rectangular microchannels with electrokinetic effects. *Int. J. Heat Mass Trans* **41**, 4229–4249.